LAWRENCE
LIVERMORE
NATIONAL
LABORATORY

LLNL-JRNL-663742

Hugoniot Experiments with Unsteady Waves

D. E. Fratanduono, D. H. Munro, P. M . Celliers, G. W. Collins

November 4, 2014

Journal of Applied Physics

Disclaimer

Hugoniot Experiments with Unsteady Waves

D. E. Fratanduono, D. H. Munro, P. M. Celliers and G. W. Collins

Lawrence Livermore National Laboratory

(Dated: September 4, 2014)

Abstract

Recent development of transparent shock wave standard materials, such as quartz, enables continuous tracking of shock waves using optical velocimetry, providing information on shock wave steadiness and pressure perturbations in the target. From a first order perturbation analysis, we develop a set of analytical formulas that connect the pressure perturbations at the drive surface to the shock velocity perturbations observed in measurements. With targets that incorporate a calibrated transparent witness material, such as quartz, and with the analytical formulas describing the perturbation response, it is possible determine the sound speed and Grüneisen coefficient of an unknown sample by using evolution of the non-steady perturbations as a probe. These formulas can also be used to improve the accuracy of traditional shock wave impedance match Hugoniot experiments of opaque samples driven with non-steady waves.

I. INTRODUCTION

Hugoniot experiments are an important means of producing high-pressure data that can be used to benchmark and test modern equation of state (EOS) models. Recently developed facilities such as the National Ignition Facility[1] (NIF), the Z-Machine[2], the OMEGA[3] facility and the Laser Mega-Joule (LMJ) facility[4] are capable of producing high-pressure shock states well into the TPa regime where little experimental data exists.[5,6] Advances in diagnostic techniques to probe those states[7–9] have enabled accurate measurement of shock states at these conditions in transparent samples with reflective shocks (e.g. Quartz[5,6] and LiF[10]). Optical velocimetry enables the measurement of shock velocities in transparent materials to better than 1% with temporal resolution less than 100 ps.

The input pressure drives generated by these new facilities often produce perturbations at the drive source that are transmitted through the target and observed as velocity perturbations at the shock front in transparent materials. Here, we develop formulas that relate pressure perturbations launched at the drive surface to the velocity perturbations observed later at the shock front. The formulas show how the arrival times and amplitudes of the perturbations observed at the shock front depend on both the sound speed and Grüneisen coefficient (i.e. the thermodynamic derivatives) of the shocked material. These formulas provide a means to extract the sound speed and Güneisen coefficient of unknown samples for appropriately designed experiments. A second important application of these formulas is to correct for non-steadiness in traditional Hugoniot experiments, where the wave speed is determined from a transit time through an opaque sample. Systematic measurement errors attributed to shock wave non-steadiness can thus be reduced significantly.

To illustrate how drive perturbations affect Hugoniot experiments, consider the typical target for an impedance matching experiment to determine the shock wave Hugoniot of an unknown sample as illustrated in Figure 1(a). In this arrangement, a shock wave is transmitted from a material with known EOS (the reference) into the unknown sample. The reference and the sample are opaque; velocities are obtained from transit time. The experiment is designed to produce two observables: (i) the shock speed in the reference and (ii) the shock speed in the unknown sample. Provided the EOS of the reference is known, the shock state in the sample is determined from impedance-matching analysis.[11–14] For transparent witness materials (such as quartz), the shock speed speed is measured continuously using optical velocimetry. However, many samples (e.g. metals) are not transparent; the shock speed in the sample is determined only from an observed transit time and

known thickness, providing an average shock speed (see Figure 1). This technique is commonly employed in gas-gun experiments where the shock velocities are steady. In the case that the shock is not steady, a systematic error may arise if the analysis is based on the assumption of steady well-defined shock states. By using the information contained in the continuous measurement of shock speed in a transparent witness, one may accurately reconstruct the two observables required for the analysis even when the shock is not steady.

Non-steadiness in the shock wave is caused, in part, by variations in the pressure drive of the experiment, such as by perturbations in the power source, or by a slightly increasing or decreasing trend owing to features of the drive platform. In the discussion to follow, consider perturbations (δp) in the pressure drive that are small relative to the average drive pressure $\langle p \rangle$. These perturbations propagate as sound waves through the shocked material and are subject to both amplitude and frequency modulations. For example, when a perturbation passes through an interface between different media, the amplitude changes due to impedance differences. A perturbation undergoes Doppler shifts as it interacts with other wave fronts, such as a shock front or rarefaction wave moving through the target. These modulations are evaluated using standard wave propagation concepts to account for the different interactions encountered by a perturbation as it propagates from the drive surface up to the leading shock front.[2,5]

Figure 1(b) illustrates how drive pressure perturbations propagate through the transparent witness until they overtake the leading shock (marked "S"). The observed shock velocity fluctuates in response to the drive perturbations, but at a much lower frequency owing to the Doppler effect of the receding shock front. The frequency of these perturbations at the shock front is governed in part by the sound speed of the material as well as the Doppler effect. Figure 1(c) shows the same set of perturbations applied to the sample side of the target. Here, they pass through a rarefaction wave (marked "R"), followed by a material interface (marked "I") until they reach the shock front in the sample (marked "S"). The Lagrangian coordinate system used in Figure 1 is a natural system for visualizing the interactions: the perturbations appear to refract as they pass through "RS", "R," and "I". Assuming that both the witness and the sample experience a common set of drive pressure perturbations, one can account for the perturbations experienced by an opaque sample as long as those perturbations are measured in a transparent witness.

In this work, we develop the formulas needed to account for drive perturbations in shock wave experiments. The formulas apply to acoustic wave propagation through fluid media which do not support shear stress. Section II describes Doppler effects on the perturbations. Section III

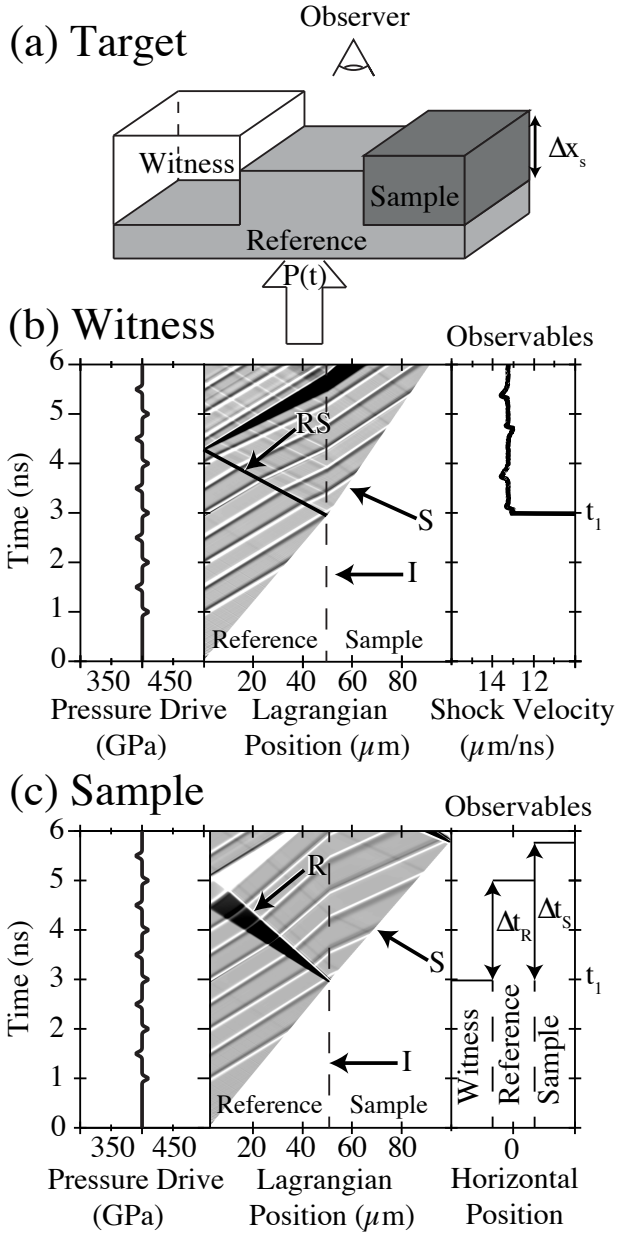

FIG. 1: Impedance matching experiment for an opaque sample. (a) Witness and sample are placed at a common plane on the reference at a known thickness from the drive surface. The observer measures the *in situ* shock velocity in the transparent witness and the timing of breakout events in each material. The pressure drive ($P(t)$), with temporal perturbations, is applied across the entire common drive surface. (b) Hydrocode simulation of the input pressure drive (shown on left) through the witness and sample in the Lagrangian frame of reference. The material interface is denoted by the dashed line and labeled "I." The observed shock velocity in the witness is marked "S" and that velocity is shown on the right. The reflected shock into the reference is marked "RS." (c) Hydrocode simulation of the same pressure drive in (b) (shown on left) through the reference and sample. The material interface is marked "I" and the shock velocity in the sample is marked "S" and the rarefaction generated in the reference is marked "R." In this case, the only observable is the time the shock exits the sample (as shown on the right). The transit time through the

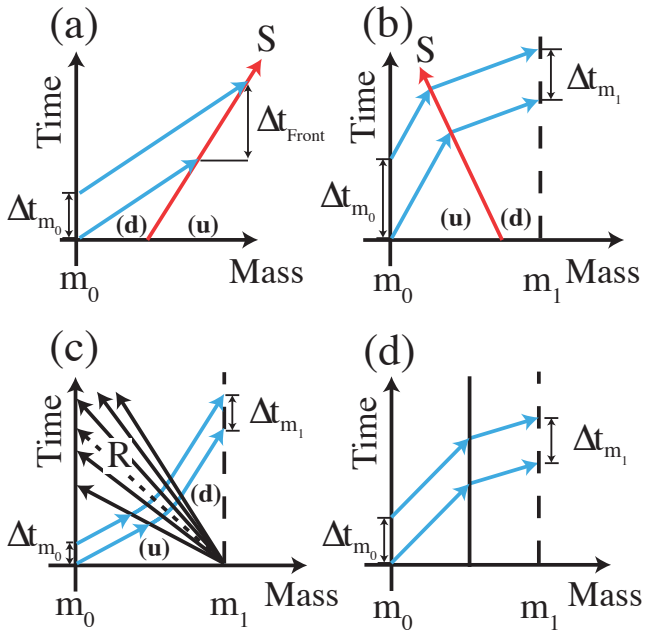

FIG. 2: Propagation paths of two acoustic perturbations (shown in blue) that originate from the same fluid element at two different times as they interact with different features of the target. (a) A receding shock front (shown in red and labeled "S"): the inter pulse interval increases in the reference frame of the shock since the front is moving away from the source (red shift). (b) Perturbations transmitted through a counter-propagating shock front (shown in red and labeled "S"): the inter pulse interval is smaller downstream than in the upstream region (blue shift). (c) Perturbations transmitted through a centered rarefaction wave (shown in black and labeled "R"): the inter pulse interval in the downstream region is greater than in the upstream region. The centered rarefaction behaves like a sharp front (dashed line). (d) There is no Doppler effect across a material interface (shown in black) since the adjacent regions share the same reference frame.

discusses how the amplitudes of perturbations are modified as they pass through wave fronts and interfaces in the flow. Section IV develops the corrections for Hugoniot experiments with an unsteady pressure drive and the validity of this model is examined through comparison with hydrocode simulations. Finally, Section V, extends these ideas to extract the sound speed and Grüneisen coefficient along the Hugoniot of a sample material using the information contained in the velocity time history of a non-steady shock front.

II. DOPPLER EFFECTS

Acoustic perturbations that are generated at a loading surface downstream of a shock front will eventually overtake the shock front. For a shock front receding from the loading surface, the arrival times of a set of perturbations at that front are much more widely spaced than at the launch surface, owing to the Doppler effect. Additional Doppler effects come about due to the interaction of the perturbations with other wave fronts in the flow. This section focuses on the various Doppler effects that are encountered by acoustic perturbations as they pass through wave fronts and interfaces entrained in the flow. The analysis that follows is carried out in planar geometry, mass-time (*m*-*t*) coordinate space, closely related (but not identical) to the Lagrangian coordinate space used in Figure 1. The mass coordinate is defined from the density distribution of fluid elements through the relation $m(x) = \int_{x_0}^{x} \rho(x)dx$ where x_0 is the position of the leftmost fluid element. The coordinate m has physical significance because $\Delta m = m_1 - m_0$ gives the areal mass contained in the fluid layer located between m_1 and m_0. Waves propagate through this coordinate space at velocity $dm/dt = \dot{m} = \rho u_f$, where ρ is the local material density upstream of the wave and u_f is the velocity of the wave relative to the upstream medium.[32] For example, acoustic perturbations propagate at the rate ρc_s in *m* - *t* coordinates, where ρ is the local density and c_s is the local Eulerian sound speed. In the *m* - *t* coordinate system, material interfaces do not propagate ($\dot{m} = 0$); they follow vertical paths. To understand the various Doppler effects, the arrival time spacings Δt of a pair of perturbations propagating through *m* - *t* space are examined as they pass through material interfaces, or interact with a waves entrained in the flow such as shocks and rarefactions. As shown in Figure 2, there are four different cases to be considered.

Before examining Figure 2 in detail, it is useful to note the formulas developed below make use of Mach numbers. A Mach number is associated with a wave front, and is defined as the ratio of the wave front velocity to the local sound speed. In the diagrams shown, wavefronts form boundaries between regions with well-defined parameters (e.g. pressure p, density ρ, sound speed c_s, particle speed u_p, etc.) The local sound speed is different on each side of the wave front, for example, the material flowing into the wave front (the upstream material) has a different sound speed from the material flowing away from the wave front (the downstream material). Therefore, one can associate two Mach numbers with each wave front corresponding to the upstream and downstream flow regions. To aid the reader, subscripts will be used to denote regions and wavefronts. Subscripts associated with Mach numbers will reference the wavefront ("S" for shock and

"R" for a centered rarefaction wave) accompanied with either a "u" for upstream of the wavefront or "d" for downstream of the wavefront. Subscripts associated with thermodynamic variables will reference flow regions.

A. Perturbations at shock fronts

Perturbations arriving at a shock front are Doppler shifted. The perceived arrival time spacing in a reference frame fixed to the front is different from the launch time spacing when they are launched from a fixed material layer. Specifically, the time interval Δt_{Front} observed in the shock frame between a pair of perturbations launched with time interval Δt_{m_0} from the point m_0 and reaching the shock after traveling through a region of uniform flow is

$$\Delta t_{\text{Front}} = \frac{\Delta t_{m_0}}{1 \mp M_S}, \tag{1}$$

where the Mach number is defined as $M_S = u_f/c_s = \dot{m}/\rho c_s$. The minus sign applies to the case of an acoustic perturbation propagating in the same direction as the shock front (overtaking it from the downstream region, $M_{S,d} < 1$) as shown in Figure 2(a). The plus sign applies for a counter-propagating acoustic perturbation (in either the upstream or downstream regions) as shown in Figure 2(b). The resulting delay between the perturbations at the counter-propagating shock shown in Figure 2(b) is

$$\Delta t_{\text{Front}} = \frac{\Delta t_{m_0}}{1 + M_{S,u}}. \tag{2}$$

In most cases, the time dilation factors corresponding to a pair of disturbances launched from m_0 and arriving later at m_1 after passing through the counter-propagating shock are required. Here the dilation factor for the transmitted acoustic disturbances is

$$\frac{\Delta t_{m_1}}{\Delta t_{m_0}} = \frac{1 + M_{S,d}}{1 + M_{S,u}}, \tag{3}$$

since $\Delta t_{m_0}/\Delta t_{\text{Front}} = (1 + M_{S,u})$ and $\Delta t_{m_1}/\Delta t_{\text{Front}} = (1 + M_{S,d})$. It is useful to note that $M_{S,u} > 1$ and $M_{S,d} < 1$, so $\Delta t_{m_1} < \Delta t_{m_0}$.

B. Perturbations propagating through rarefactions

The case of a counter-propagating centered rarefaction is shown in Figure 2(c). The rarefaction is centered at the point (m_1, t_0), and the fan of reversed-sloped lines radiating from (m_1, t_0) corresponds to an array of characteristics with the slope magnitudes equal to the local value of ρc_s. The

fan divides two regions of uniform flow: upstream and downstream. The leading (upstream) edge of the rarefaction propagates along the line $m_{R,u}(t) = m_1 - |\dot{m}_u|(t - t_0)$, while the trailing (downstream) edge propagates along $m_{R,d}(t) = m_1 - |\dot{m}_d|(t - t_0)$, where $\dot{m}_u = \rho_u c_{su} > \dot{m}_d = \rho_d c_{sd}$. Upstream of the rarefaction fan forward-directed perturbations propagate with slope $+|\dot{m}_u|$, while downstream they propagate with slope $+|\dot{m}_d|$. Inside the fan, the forward-directed (counter-propagating) sound waves follow curved paths with slope $dm/dt = -(m - m_1)/(t - t_0)$. This equation defines a family of hyperbolas $m(t) = (m_1(t - t_0) - C)/(t - t_0)$, where C is a parameter associated with each hyperbola. When any forward-going characteristic is extrapolated from the upstream and downstream regions into the rarefaction fan, the intersections occur along the line $m = m_1 - \sqrt{\dot{m}_d \dot{m}_u}(t - t_0)$. Therefore, for the purpose of computing Doppler shifts, the rarefaction fan is equivalent to a sharp front moving at the rate $\sqrt{\dot{m}_u \dot{m}_d}$. The effective Mach numbers are $M_{R,d} = 1/M_{R,u} = \sqrt{\dot{m}_u/\dot{m}_d}$. This front is illustrated as the dashed line (sharp front solution) in Figure 2(c). Similar to the case of perturbations transmitted through a counter-propagating shock, the dilation factor for a pair of acoustic disturbances transmitted through a counter-propagating rarefaction from a fluid element in region 0 to an element in region 1 is

$$\frac{\Delta t_{m_1}}{\Delta t_{m_0}} = \frac{1 + M_{R,d}}{1 + M_{R,u}} = \sqrt{\frac{\rho_u c_{su}}{\rho_d c_{sd}}}. \tag{4}$$

In this case, $M_{R,u} < 1$ and $M_{R,d} > 1$, so $\Delta t_{m_1} > \Delta t_{m_0}$.

C. Perturbations propagating through material interfaces

The final case to consider is the interaction of acoustic perturbations through a material interface as shown in Figure 2(d). Since the material interface is stationary in mass-time coordinates (there is no flow), no Doppler shift is imparted upon the perturbations and

$$\frac{\Delta t_{m_1}}{\Delta t_{m_0}} = 1. \tag{5}$$

D. The Doppler shifts through complex targets

To illustrate how these results are used to relate the time history of perturbations observed at the leading shock front to their time history near the drive surface consider the case shown in Figure 3, where a steady shock wave has traveled through three different materials denoted as A, B and C. The impedance of material A is greater than material B which results in a centered rarefaction

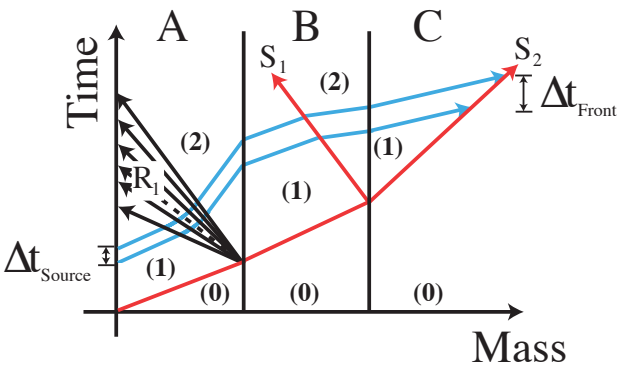

FIG. 3: Propagation of acoustic perturbations, shown in blue, traveling through three different material layers denoted as A, B and C. The impedance of material A and C are greater than material B. When the shock front, shown in red, enters material B a centered rarefaction wave (labeled "R1"), shown in black, is generated in material A. Further, when the shock enters material C, a counter propagating shock (labeled "S1") is generated in material B, shown in red. The shock front in material C is labeled as "S2." Regions of constant flow are labeled numerically.

in sample A when the shock enters material B. Further, the impedance of material B is less than than material C which generates a counter-propagating shock in material B. Using Equations (1-5), the time dilation factor relating the inter pulse separation of events at the source (Δt_{Source}) to the corresponding events on the shock front (Δt_{Front}) is given by

$$\frac{\Delta t_{\text{Front}}}{\Delta t_{\text{Source}}} = \frac{1+M_{R1,d}}{1+M_{R1,u}} \frac{1+M_{S1,d}}{1+M_{S1,u}} \frac{1}{1-M_{S2,d}}. \tag{6}$$

where the subscript denotes the wavefronts and the upstream or downstream regions. In the next section, expressions for the transmission coefficients of the perturbation amplitudes as they propagate through the features are derived, as illustrated in Figure 2.

III. FIRST ORDER HYDRODYNAMICS

The magnitudes of acoustic perturbations change as they pass through wave fronts and interfaces because the impedance of the medium changes across each of these features. This section focuses on the transmission coefficients of the perturbation amplitudes as they propagate through the flow. The analysis is based on first-order approximations of the acoustic perturbations. The pressure p and fluid velocity u can be approximated as: $p(t) = \langle p \rangle + \delta p(t)$ and $u(t) = \langle u \rangle + \delta u(t)$,

where $\langle p \rangle$ and $\langle u \rangle$ are time-averaged values. Similar to the Doppler analysis, consider the four cases sketched in Figure 4.

A. Acoustic interactions with a shock

An acoustic wave is either be reflected (if it overtakes a shock front), Figure 4(a), or transmitted (through a counter-propagating shock) Figure 4(b). Either interaction results in the generation of a non-propagating isobaric density perturbation and causes a perturbation in shock speed. The non-propagating density disturbance follows a vertical path in m - t coordinates, and produces a zone of modified entropy downstream of the shock. These are denoted as the solid black lines in Figure 4(a) and 4(b).

There are four possible perturbation modes to consider: downstream of the shock there are two acoustic waves δp_- and δp_+ representing waves receding from and approaching the shock, respectively;[33] there is a non-propagating density disturbance $\delta\rho_x$; and, upstream of the shock there can be a counter-propagating acoustic wave δp_u. The downstream pressure, density, and velocity perturbations are related through: $\delta p = \delta p_+ + \delta p_-$, $\delta\rho = \delta p/c_d^2 + \delta\rho_x$, and $\rho_d c_d \delta u = \delta p_+ - \delta p_-$. On the upstream side, the perturbations are all simply related to the upstream counter-propagating perturbation $\delta p = \delta p_u$, $\delta\rho = \delta p_u/c_u^2$, and $\rho_u c_u \delta u = \delta p_u$.

First-order jump conditions at the shock front are needed to relate all four mode amplitudes, $\delta p_+, \delta p_-, \delta\rho_d$, and δp_u, to each other. The easiest jump condition is the first-order Hugoniot. The shock front always satisfies the Hugoniot condition,

$$e_u - e_d = (1/\rho_d - 1/\rho_u)(p_d + p_u)/2, \tag{7}$$

where e is the thermodynamic internal energy per unit mass and the subscripts u and d refer to upstream and downstream quantities respectively. In first order, this is

$$(e_{pd} - \Delta v/2)\delta p_d + (e_{\rho d} - \bar{p}/\rho_d^2)\delta\rho_d - (e_{pu} + \Delta v/2)\delta p_u - (e_{\rho u} - \bar{p}/\rho_u^2)\delta\rho_u = 0$$

where $e_p = (\partial e/\partial p)_\rho$, $e_\rho = (\partial e/\partial\rho)_p$, $\bar{p} = (p_d + p_u)/2$, and $\Delta v = 1/\rho_u - 1/\rho_d > 0$. The derivatives of internal energy per unit mass with respect to pressure (e_p) and density (e_ρ) satisfy the thermodynamic relationship,

$$e_\rho = p/\rho^2 - c^2 e_p. \tag{8}$$

The first order Hugoniot takes the form, in terms of the upstream and downstream Mach numbers $M_{S,u} > 1$ and $M_{S,d} < 1$,

$$(e_{pd} - \Delta v/2)\delta p_d - (e_{pd} - M_{S,d}^2 \Delta v/2) c_d^2 \delta\rho_d - (e_{pu} + \Delta v/2)\delta p_u + (e_{pu} + M_{S,u}^2 \Delta v/2) c_u^2 \delta\rho_u = 0. \quad (9)$$

The first-order Hugoniot leads to the following the constraint among the four modes, δp_+, δp_-, $\delta\rho_x$, and δp_u,

$$(1 - M_{S,d}^2)(\delta p_+ + \delta p_-) + (2e_{pd}/\Delta v - M_{S,d}^2) c_d^2 \delta\rho_x + (M_{S,u}^2 - 1)\delta p_u = 0. \quad (10)$$

The other two jump conditions at the shock front are conservation of mass and momentum. In shock-fixed coordinates, $p + \rho u^2$ is constant across the shock front. The differential form is $\delta p + u^2 \delta\rho + 2\rho u(\delta u_s - \delta u)$, since the change in velocity is due to both the change in shock speed (δu_s) and the change in fluid speed (δu). Since $\dot{m} = \rho u$ is constant across the front and δu_s is equivalent for upstream and downstream flow, the first-order momentum balance requires that the quantity $\delta p + u^2 \delta\rho - 2\rho u \delta u$ is conserved across the shock front. This provides a second constraint on the four mode amplitudes,

$$(1 - M_{S,d})^2 \delta p_+ + (1 + M_{S,d})^2 \delta p_- + M_{S,d}^2 c_d^2 \delta\rho_x = (1 + M_{S,u})^2 \delta p_u. \quad (11)$$

The differential form of mass conservation does not impose any further constraints among the four mode amplitudes. However, it does determine the first-order change in shock speed (δu_s). The differential form of ρu is $u\delta\rho + \rho(\delta u_s - \delta u)$, which determines δu_s:

$$\begin{aligned}(\rho_d - \rho_u) c_d \delta u_s = {} & (1 - M_{S,d})\delta p_+ - (1 + M_{S,d})\delta p_- \\ & - M_{S,d} c_d^2 \delta\rho_x - (c_d/c_u)(1 - M_{S,u})\delta p_u.\end{aligned} \quad (12)$$

The two equations (10) and (11) relating the four first-order modes (δp_+, δp_-, $\delta\rho_x$, and δp_u) can be used in this case to determine the unknown reflected wave (δp_-) and non-propagating density disturbance ($\delta\rho_x$). The observable perturbation in the shock front velocity may then be obtained from equation (12). In matrix form, the system to solve is

$$\begin{aligned}&\begin{bmatrix} (1 + M_{S,d})^2 & M_{S,d}^2 \\ (1 - M_{S,d}^2) & 2e_{pd}/\Delta v - M_{S,d}^2 \end{bmatrix} \begin{pmatrix} \delta p_- \\ c_d^2 \delta\rho_x \end{pmatrix} \\ &= \begin{bmatrix} -(1 - M_{S,d})^2 & (1 + M_{S,u})^2 \\ -(1 - M_{S,d}^2) & (M_{S,u}^2 - 1) \end{bmatrix} \begin{pmatrix} \delta p_+ \\ \delta p_u \end{pmatrix}\end{aligned} \quad (13)$$

and the solution is

$$\begin{aligned}\delta p_- =& -\frac{1-M_{S,d}}{1+M_{S,d}}\frac{(1-M_{S,d})e_{pd}-M_{S,d}^2\Delta v}{D}\,\delta p_+ \\ &+\frac{1+M_{S,u}}{1+M_{S,d}}\frac{(1+M_{S,u})e_{pd}-M_{S,u}M_{S,d}^2\Delta v}{D}\,\delta p_u,\end{aligned} \tag{14}$$

$$\begin{aligned}c_d^2\delta\rho_x =& -\frac{2M_{S,d}(1-M_{S,d})\Delta v}{D}\,\delta p_+ \\ &+\frac{(M_{S,u}+1)(M_{S,u}M_{S,d}-1)\Delta v}{D}\,\delta p_u,\end{aligned} \tag{15}$$

where

$$D=(1+M_{S,d})e_{pd}-M_{S,d}^2\Delta v. \tag{16}$$

The shock front velocity takes the form

$$(\rho_d-\rho_u)c_d\delta u_s=\frac{2(1-M_{S,d})e_{pd}}{D}\,\delta p_+ +\,(M_{S,u}+1)\left(\frac{\rho_u M_{S,u}}{\rho_d M_{S,d}}-\frac{(M_{S,u}+1)e_{pd}-M_{S,d}\Delta v}{D}\right)\delta p_u. \tag{17}$$

Now, consider the two specific cases of a sound wave over taking a shock front from behind and a sound wave transmitted through a counter-propagating shock front as illustrated in Figure 4(a-b).

1. *Sound wave overtaking a shock*

For the case of a sound wave incident on a shock from behind, the approaching sound wave δp_+ is known. There are no upstream modes ($\delta p_u = 0$). The reflected sound wave (δp_-) and isobaric density perturbation ($\delta\rho_x$) are the unknowns. Equation (17) is used to determine changes in the shock strength due to the acoustic perturbations. Since $\delta p_u = 0$ and $\delta p_+ = \rho_d c_d \delta u_+$, equation (17) becomes

$$\frac{\delta u_s}{\delta u_+}=\frac{-2\eta}{\eta-1}\frac{M_{S,d}-1}{1+M_{S,d}-(\eta-1)M_{S,d}^2\Gamma_d}, \tag{18}$$

where $\eta=\rho_d/\rho_u$ is the compression ratio across the shock and $\Gamma_d=(1/\rho_d)(\partial p/\partial e|_\rho)_{S,d}$ is the Grüneisen coefficient in the downstream flow of the shock compressed material.

2. *Sound wave transmitted through a shock*

For the case of a sound wave passing through a counter-propagating shock (Figure 4(b)), there are no downstream waves approaching the shock ($\delta p_+ = 0$), while δp_u is given. This simplifies

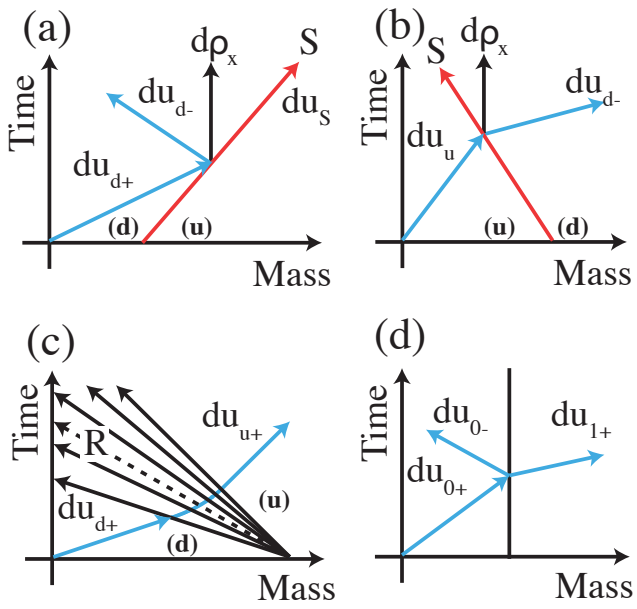

FIG. 4: Interactions of acoustic perturbations with wavefronts or interfaces in the m-t plane. Downstream and upstream regions are denoted by "d" and "u", respectively. (a) Perturbations overtaking a receding shock front (shown in red and labeled "S"). (b) Perturbations transmitted through a counter-propagating shock front (shown in red and labeled "S"). (c) Perturbations transmitted through a counter-propagating centered rarefaction wave (shown in black and labeled "R"). (d) Perturbations transmitted through a material interface (black line).

the evaluation of equations (14 - 17). The relationship between the amplitude of the acoustic wave before and after interaction with the shock front is required ($\delta u_- / \delta u_u$). Recall that $\delta p_u = \rho_u c_u \delta u_u$ and $\delta p_- = \rho_d c_d \delta u_-$. From equation (14),

$$\frac{\delta u_-}{\delta u_u} = M_{S,d} \frac{M_{S,u}+1}{M_{S,d}+1} \frac{1+M_{S,u}^{-1}-(\eta-1)M_{S,d}^2\Gamma_d}{1+M_{S,d}-(\eta-1)M_{S,d}^2\Gamma_d}. \tag{19}$$

B. Transmission through a centered rarefaction

A pressure perturbation propagating through a centered rarefaction wave, shown in Figure 4(c), does not reflect as it propagates down the rarefaction. In smooth flow, such as in a rarefaction wave, the Riemann invariants, $\sigma \pm u$, are conserved for propagating acoustic waves. Here σ is the thermodynamic function defined by $\sigma = \int 1/\rho c_s dp$. The quantity $\sigma + u$ is constant for an acoustic disturbance propagating downstream through the rarefaction fan, while $\sigma - u$ is constant

for an acoustic disturbance propagating upstream. For the zero-order flow ($\delta p = 0$ and $\delta u = 0$), the downstream Riemann invariants reduce to $\sigma_u + u_u = \sigma_d + u_d$. For a centered rarefaction wave, the upstream Riemann invariants satisfy $\sigma - u = constant$ everywhere. Therefore, $\delta\sigma_u - \delta u_u = 0$, $\delta\sigma_d - \delta u_d = 0$ throughout the rarefaction. In addition, the downstream invariants must satisfy the relation $\delta\sigma_u + \delta u_u = \delta\sigma_d + \delta u_d$. Combining these relationships leads to the conclusion that $\delta\sigma$ and δu have to be preserved independently as the perturbation travels down the rarefaction: $\delta\sigma_d = \delta\sigma_u$, and $\delta u_d = \delta u_u$. The transmission coefficient for the pressure perturbation is therefore,

$$\frac{\delta p_{d+}}{\delta p_{u+}} = \frac{\rho_d c_{sd}}{\rho_u c_{su}}, \tag{20}$$

and the transmission coefficient for the corresponding velocity perturbation is

$$\frac{\delta u_{d+}}{\delta u_{u+}} = 1. \tag{21}$$

C. Transmission through a material interface

Perturbations incident at a material interface will encounter a change in impedance, which results in transmitted and reflected components. At the interface, the pressure (δp) and velocity (δu) perturbations must be continuous, owing to momentum and mass conservation. The acoustic impedance is the ratio $\delta p/\delta u = \pm\rho c_s$, where the sign depends on the direction of wave propagation ($+$ for propagation along increasing m). From the impedance of the medium, the total acoustic pressure is $\delta p = \rho c_s(\delta u_+ - \delta u_-)$ while the total acoustic velocity is $\delta u = (\delta p_+ - \delta p_-)/(\rho c_s)$. At a material interface, the incident (i), reflected (r), and transmitted (t) waves are related by $\delta p_i + \delta p_r = \delta p_t$ and $\delta u_i + \delta u_r = \delta u_t$. From these relationships, one may show that the transmission coefficient for a pressure perturbation is

$$\frac{\delta p_{1+}}{\delta p_{0+}} = \frac{2\rho_1 c_{s1}}{\rho_1 c_{s1} + \rho_0 c_{s0}}, \tag{22}$$

and the transmission coefficient for the corresponding velocity perturbation is,

$$\frac{\delta u_{1+}}{\delta u_{0+}} = \frac{2\rho_0 c_{s0}}{\rho_1 c_{s1} + \rho_0 c_{s0}}, \tag{23}$$

where the perturbation is transmitted from material 0 to material 1. Note that in this case the material regions are not labeled as upstream and downstream since there are no moving fronts in the mass-time frame of reference.

D. The transmission coefficients of complex targets

The amplitudes of the perturbations at the source (δu_{A0}) and the shock front (δu_{Front}), shown in Figure 3, are related through equations (14), (17), (21) and (23). The transmission coefficients through the centered rarefaction in material A are determined from equation (21),

$$\frac{\delta u_{A2}}{\delta u_{\text{Source}}} = 1. \tag{24}$$

The transmission coefficient of each material interface (equation (23)) is

$$\frac{\delta u_{B1}}{\delta u_{A2}} = \frac{2\rho_{A2}c_{s,A2}}{\rho_{B1}c_{s,B1} + \rho_{A2}c_{s,A2}}, \tag{25}$$

and

$$\frac{\delta u_{C1}}{\delta u_{B2}} = \frac{2\rho_{B2}c_{s,B2}}{\rho_{C1}c_{s,C1} + \rho_{B2}c_{s,B2}}. \tag{26}$$

For the counter-propagating shock front in material B, apply equation (19) to determine the transmission coefficient,

$$\frac{\delta u_{B2}}{\delta u_{B1}} = M_{S1,d}\frac{M_{S1,u}+1}{M_{S1,d}+1}\frac{1+M_{S1,u}^{-1}-(\eta_B-1)M_{S1,d}^2\Gamma_{B2}}{1+M_{S1,u}-(\eta_B-1)M_{S1,d}^2\Gamma_{B2}}, \tag{27}$$

where $\eta_B = \rho_{B2}/\rho_{B1}$. Finally, for the receding shock in material C, equation (18) is applied,

$$\frac{\delta u_{\text{Front}}}{\delta u_{C1}} = \frac{-2\eta_C}{\eta_C - 1}\frac{M_{S2,d}-1}{1+M_{S2,d}-(\eta_C-1)M_{S2,d}^2\Gamma_{C1}}, \tag{28}$$

where $\eta_C = \rho_{C1}/\rho_{C0}$. The total transmission coefficient is obtained by multiplying the coefficients from each of these individual interactions to relate particle velocity perturbations launched at the source (δu_{Source}) to the shock velocity variations observed at the shock front (δu_{Front}).

IV. APPLICATION TO IMPEDANCE MATCHING EXPERIMENTS

A. Linear scaling transformation

Impedance matching experiments relate the reference and sample equation of states. Experiments typically measure the slope of the two Rayleigh lines ($\rho_0 u_s$), proportional to the shock speeds in the reference and sample. For opaque materials, the transit times through known samples thicknesses are observed, which represent the time averaged shock velocities. In those experiments, a systematic uncertainty in the impedance matching shock state results if the shock velocity

is not steady in both materials. However, witness measurements can be used to estimate how the shock speed fluctuates in both the sample and reference and thereby correct for wave unsteadiness in the impedance matching analysis. As shown previously, observed perturbations in the witness are directly related to perturbations in the reference and the sample. The time history of acoustic perturbations at the drive surface can be directly related to perturbations observed at the shock front through linear scaling of the time coordinate by an appropriate time dilation factor

$$\frac{\Delta t_{\text{Front}}}{\Delta t_{\text{Source}}} = f, \tag{29}$$

as shown in Section II D. Similarly, the amplitude of perturbations launched at the drive surface can be related to the perturbation amplitude observed at the shock front through another linear scaling factor,

$$\frac{\delta u_{\text{Front}}}{\delta u_{\text{Source}}} = g, \tag{30}$$

as shown in Section III D. Here f and g are constants that can be computed from the target geometry, material properties and the shock states as described by equations (1), (3) to (5), (14), (18), (19), (21) and (23).

For a two section target, where the input pressure drive is identical for both sections, one can relate the time histories of perturbations occurring at the leading shock front in each section through a ratio of dilation factors,

$$\frac{\Delta t_{\text{AFront}}}{\Delta t_{\text{BFront}}} = \frac{f_{\text{A}}}{f_{\text{B}}} = F, \tag{31}$$

and the similarly the ratio of amplitudes of shock front velocity variation is related through the ratio of transmission coefficients,

$$\frac{\delta u_{\text{AFront}}}{\delta u_{\text{BFront}}} = \frac{g_{\text{A}}}{g_{\text{B}}} = G, \tag{32}$$

where F and G are also constants. The relation between the shock front velocity histories observed at the shock fronts passing through the the witness and sample can be expressed through a linear scaling transformation,

$$\delta u_{A\text{Front}}(t - t_{AB}) = G \times \delta u_{B\text{Front}}((t - t_{AB})F^{-1}) \text{ for } t \geq t_{AB}, \tag{33}$$

where the factors F and G can be computed using the techniques outlined above, and t_{AB} is the time when the shock passes from the common baseplate into the separate A and B material segments. Using equation (33), the shock velocity time history in an opaque material, $u_{A\text{Front}}(t)$, is estimated provided a continuous measurement of the time history measured in a transparent witness $u_{B\text{Front}}(t)$ is available.

B. Non-Steady Wave Correction

To understand how this linear scaling transformation is used in impedance matching experiments, return to the case shown in Figure 1. In that experiment, the average shock velocities in the reference and the sample from transit time measurements, $\langle u_{\mathrm{ref}} \rangle$ and $\langle u_{\mathrm{sample}} \rangle$ and a continuous shock velocity measurement in the witness material $u_{\mathrm{W}}(t)$ are observed. The shock passes from the reference material into the sample and the witness at time t_1 and the shock transit time in the reference and the sample are Δt_{R} and Δt_{S}, respectively. The first-order correction parameters needed to evaluate equation (33) are computed separately for the sample and reference (both relative to the witness), using the methods outlined above. Using equation (33) one may show that

$$\delta u_{\mathrm{S}}^{*}(t-t_1) = G_{\mathrm{S}} \delta u_{\mathrm{W}}((t-t_1)F_{\mathrm{S}}^{-1}) \text{ for } t \geq t_1, \tag{34}$$

The superscript $(*)$ denotes values estimated from the continuous shock velocity witness measurement, $\delta u_{\mathrm{W}}(t)$, which represents the velocity perturbations about the average value, $\langle u_{\mathrm{W}} \rangle$,

$$\delta u_{\mathrm{W}}(t) = u_{\mathrm{W}}(t) - \langle u_{\mathrm{W}} \rangle. \tag{35}$$

For equation (35), the average velocity in the witness, $\langle u_{\mathrm{W}} \rangle$, must contain the same temporal set of perturbations as experienced by the sample,[34]

$$\langle u_{\mathrm{W}} \rangle = \frac{\int_0^{\frac{\Delta t_{\mathrm{S}}}{F_{\mathrm{S}}}} u_{\mathrm{W}}(t-t_1)dt}{\frac{\Delta t_{\mathrm{S}}}{F_{\mathrm{S}}}}. \tag{36}$$

These corrections are combined with the measured average shock velocities $\langle u_{\mathrm{S}} \rangle$ to estimate the instantaneous shock velocities as a function of time,

$$u_{\mathrm{S}}^{*}(t-t_1) = \langle u_{\mathrm{S}} \rangle + \delta u_{\mathrm{S}}^{*}(t-t_1). \tag{37}$$

Evaluating equation (37) at time $t = t_1$ yields the instantaneous shock velocities in the sample at the moment the shock passes through the reference-sample interface. (For noisy data a suitable average over a small time interval near t_1 may be more appropriate.) A similar approach can be taken to estimate the correction for the reference. The standard impedance matching analysis is then applied to these values in order to determine the Hugoniot state in the sample. The correction vanishes for steady shocks and is proportional to the amplitude of the measured shock speed perturbations for non-steady shocks. It is important to note that the correction depends upon Mach

numbers, compression ratios, and thermodynamic derivatives for reference, sample and witness. These values are evaluated at the average shock states in the various materials using available EOS models. The uncertainties of those parameters all enter into the uncertainty to compute the correction. However, since the magnitude of the correction is small in proportion to the average velocities for a well-designed experiment, the uncertainty in the correction is usually negligible relative to other uncertainties in the experiment.

C. Model Validation using Hydrocode Simulations

The 2D arbitrary Lagrangian-Eulerian hydrodynamics code CALE[15] is used to examine the validity of the model developed here. The simulation consists of a quartz reference, quartz witness and samples with either higher (copper) or lower (water) impedance than quartz. Simulations are conducted in a 1D geometry and identical loading histories are used as inputs to both sections of the targets (sample and witness). Simulation package consists of a 100 μm quartz baseplate. Attached to the baseplate is a quartz witness and sample (either copper or water) that is 50 μm thick with a quartz anvil attached to the rear surface. The target design is shown in the inset of Figure 5. Four loading histories (constant-pressure drive, increasing-pressure drive, decreasing-pressure drive, "bump" pressure drive) are examined with random perturbations imposed. The input pressure drives are shown in Figure 5. Quartz is used as both a reference and a witness, since much work has been done recently towards its development as a standard.[5,6,16]

A Mie-Grüneisen functional form for the EOS is used in these simulations and analyses.[17] The specific form used is

$$p = \frac{\rho_0 c_0^2 \mu (1 + (1 - \Gamma_0/2)\mu)}{1 - (s-1)\mu} + \rho_0 \Gamma_0 e, \tag{38}$$

where p is the pressure, ρ_0 is the initial density of the material, $\mu = \rho/\rho_0 - 1$, e is the internal energy per unit mass, Γ_0 is the Grüneisen coefficient at ambient conditions and the parameters c_0 and s describe the principal Hugoniot of the material through the relation $u_s = c_0 + s u_p$. We assume that $\Gamma\rho = \Gamma_0\rho_0$. The EOS parameters for the various materials are provided in Table I. The Mie-Grüneisen form is based on a typical linear $u_s - u_p$ form for representing the principal Hugoniot of materials, which makes it convenient to use in the numerical tests. In general, for the impedance match standard and witness materials used in the experiment, a well-calibrated tabular model or an accurate Mie-Grüneisen fit are equally adequate for computing the correction factors, as long as accurate Hugoniot curves, sound speeds and Grüneisen coefficients are extracted from

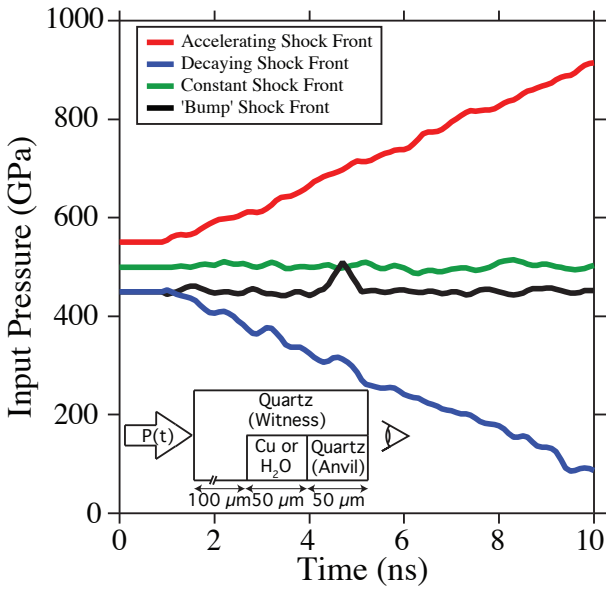

FIG. 5: Input pressure drives used in Configuration of CALE hydrocode simulations. Inset illustrates target design used in CALE simulations.

TABLE I: Hydrocode simulation parameters and approximate unsteady wave correction factors estimated from the Mie-Grüneisen EOS model evaluated for shocks states resulting from a 500 GPa steady shock in the Quartz witness.

Material	ρ_0 (g/cc)	c_0 (km/s)	s (s/km)	Γ	f @500 GPa	g @500 GPa	F @500 GPa	G @500 GPa
Quartz[5]	2.65	4.08	1.30	0.6	1.642	1.536	–	–
Copper[19,20]	8.93	3.933	1.50	2.0	1.555	1.396	0.947	0.909
Water[21,22]	1.0	2.19	1.35	0.9	1.811	1.782	1.103	1.160

the models. For an unknown sample, the principal Hugoniot may not be known and an EOS table may not exist. In this case one may start with a rough estimate of the principal Hugoniot along with an estimate of the Grüneisen coefficient *a priori* and iterate upon the assumed linear $u_s - u_p$ relation until a convergence criterion is met. An alternative is to use a generic EOS model for the sample material, such as QEOS.[18]

The results of one copper simulation using the "bump" input pressure drive, is shown in Figure 6. The quartz witness shock velocity determined from the hydrocode simulations is shown in

grey and the shock velocity passing through the quartz baseplate, copper sample, and quartz anvil velocity is shown in black. At ~ 5.91 ns, the simulations indicate that the shock exits the quartz baseplate and enters the copper sample. Since the copper has higher impedance than the quartz, a reflected shock is generated in the quartz baseplate. At ~ 9.31 ns, the shock exits the copper sample and enters the quartz anvil.

The systematic errors associated with the non-steady drives is observed by applying impedance match analysis to uncorrected data extracted from the simulations. Specifically, the average shock velocity in the sample is extracted and used in an impedance match analysis, along with the shock velocity in the quartz observed at the moment the shock enters the sample. The percent difference in density between the known Hugoniot value for the sample and the value determined from the average transit time are shown in Figure 7. A large difference between the known Hugoniot density state and that determined from the average transit time is observed in both the accelerating, decaying and "bump" input pressure drives (blue points labeled "uncorrected" in Figure 7). The error bars arise from the numerical resolution of the simulations including numerical transients (artifacts) in tracking the shock velocity at the moments when the shock crosses a material interface.

As outlined in the previous section, the (unobservable) velocity history in the Cu sample is estimated to determine a corrected velocity for the impedance match analysis. For this case, equations (1) and (3) are used to relate Doppler shifts of the quartz witness/reference to the copper sample. When the shock enters the quartz anvil, a centered rarefaction wave is generated and equation (4) is used. The amplitude of the perturbations at these fronts are related through equations (23), (21) and (19). Analytic evaluation of all these terms using the EOS model provides enough information to estimate the shock velocity in the copper sample (shown in red in Figure 6) by applying the scaling transformation of equation (33) to the quartz witness profile, and similarly so for the anvil shock velocity (shown in blue). The simple linear scaling transformation applied to the velocity history in the quartz witness provides a high fidelity estimate of the velocity profile in the Cu sample, and also the profile transmitted into the quartz anvil. The estimated velocity profiles using the scaling transformation of equation (33) are valid only while the loading history is identical for both sections of the target. When a reverberation occurs within the sample, the loading histories for the two sections are no longer identical and equation (33) is no longer valid.

In the absence of a detailed evaluation of the correction factors F and G required by equation (33), a simplified correction may be applied by assuming $F = 1$ and $G = \langle u_{\text{sample}} \rangle / \langle u_{\text{W}} \rangle$ where

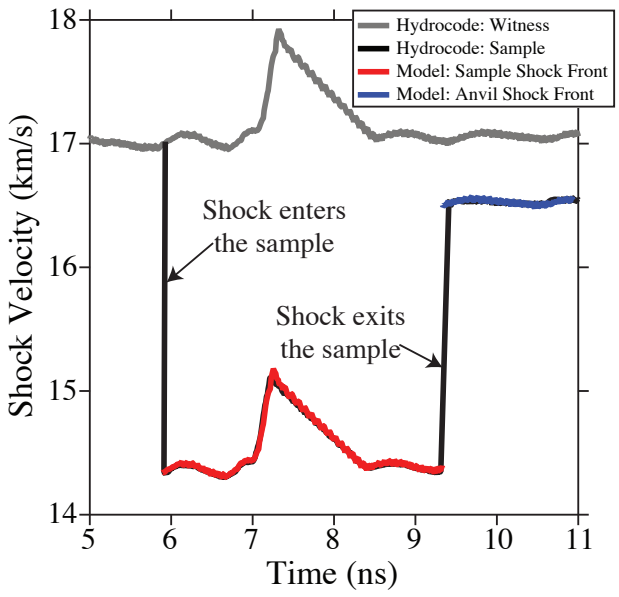

FIG. 6: Hydrocode simulations of the quartz/copper target using the "bump" input pressure drive. A non-steady input pressure generates perturbations in the observed shock velocity. The hydrocode simulated quartz witness shock velocity is shown in grey. At ~ 5.91 ns the shock enters the copper sample and exits the sample at ~ 9.31 ns, as shown in black. Application of equation 33 to the witness profile (grey) produces the estimated velocities in the sample (red) and reshock anvil (blue). Due to large "bump" in the shock velocity, the average shock velocity in the sample is greater than the shock velocity at impact (~ 5.91 ns) and would introduce a systematic error in impedance-matching analysis.

the averages are evaluated over the transit time through the sample. In Figure 7 this is referred to as the zeroth order correction, and is equivalent to assuming that the relative velocity perturbation in the sample is the same as in the witness, and that the relative time dilation factors are also the same. This correction produces the black points in Figure 7. For drives with a systematic trend (accelerating or decaying) the zero order correction does not adequately account for the wave unsteadiness and is systematically in error. In particular, for the Cu sample (high impedance) it produces results that are systematically soft for accelerating shocks, and stiff for decaying shocks. The systematics are inverted for the case of the water sample (low impedance). In contrast, the analytical form was able to correct systematic errors of up to 10% in shock density, and performs better than the zero order correction for waves with an accelerating or decelerating trend.

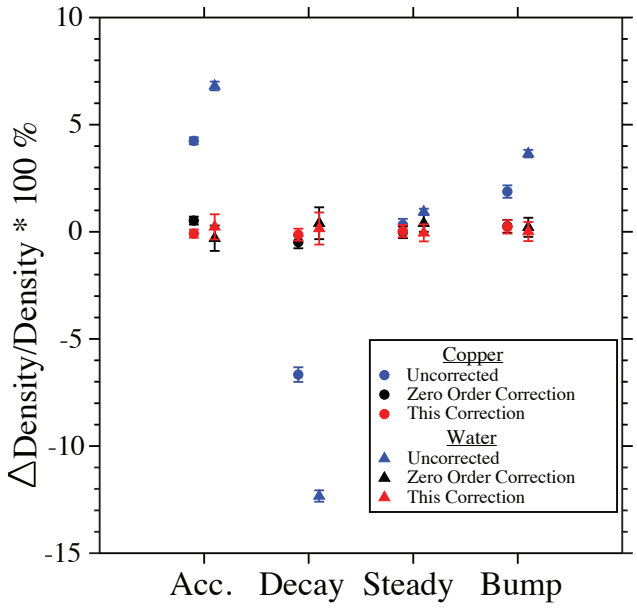

FIG. 7: The percent difference between the sample (copper as circles or water as traingles) shock density and the shock density determine from transit time measurements for four different input pressure drives. The blue points are the results obtained using the average shock velocity in the sample, the black points represent a zero order correction and the red points use the technique presented here.

V. EXTRACTING THE SOUND SPEED AND GRÜNEISEN COEFFICIENT

Shock wave Hugoniot measurements typically yield the thermodynamic parameters p, ρ and e along the Hugoniot path on the mechanical EOS surface, $p(\rho, e)$ of the sample material. Wide-ranging EOS models that are fit to Hugoniot data can be improved if information is available about states away from the Hugoniot (off-Hugoniot states) to provide further constraints on the model. This is equivalent to providing information about the local slope of the EOS surface at the Hugoniot state, as given by the orthogonal derivatives,

$$\left(\frac{\partial p}{\partial e}\right)_{\rho} = \rho\Gamma, \tag{39}$$

and

$$\left(\frac{\partial p}{\partial \rho}\right)_{e} = c_s^2 - \frac{p}{\rho}\Gamma \tag{40}$$

which depend upon the Hugoniot pressure and density, as well as the sound speed and Grüneisen coefficient. Previous determinations of sound speed and Grüneisen coefficients using off-Hugoniot data have required performing additional specialized experiments beyond Hugoniot experiments,

such as release wave experiments,[23–26] reflected shock experiments,[27,28] shock compression of porous samples,[29] wave overtake measurements,[30,31] and Mach reflection experiments.[27] In experiments with fluctuating pressure drives, the acoustic perturbations propagating behind the leading shock follow off-Hugoniot paths on the EOS surface in the neighborhood of the Hugoniot state and therefore contains information about the local EOS derivatives at the Hugoniot state. In an appropriately designed experiment, a quantitative analysis of the perturbation response of a shock wave experiment using the expressions developed in sections II and III enables extraction of both the sound speed and Grüneisen coefficient of the sample.

The linear scaling transformation represented by equation (33) provides the quantitative means to extract both sound speed and Grüneisen coefficient from a non-steady shock measurement. In section IV, the parameters F and G are computed from EOS models of the materials used in the experiment. When a pair of fluctuating signals are available by direct observation then F and G can be determined directly, provided the two signals are generated by a common source of perturbation. In this situation the signal pairs will conform to the scaling transformation represented by equation (33), so that F and G can be regarded as observables of the measurement. Standard fitting procedures can be applied to the pair of perturbation signals to determine F and G. From knowledge of the target structure, analytical expressions can be developed to relate the sound speed and Grüneisen coefficient to the measured observables F and G. The sound speed emerges through relative timing of transmitted perturbations (the F observable) and the Grüneisen coefficient from the relative amplitudes as well as the sound speed (involving both F and G). These determinations depend, in a relative sense, on the corresponding parameters of the EOS standard and witness materials used in the experiment. Accuracy of these results depends on the accuracy of our knowledge of the EOS of the standard and witness materials.

To illustrate this concept, examine the effect of drive perturbations on the shock fronts in a transparent witness and transparent sample as shown in Figure 8(a). Assume that the witness is also the reference material. The shock front is measured continuously in both the witness and the sample. When the shock enters the sample, 8(c), the shock state (p_{C1}, ρ_{C1} and $u_{p,C1}$) is determined. The arrival times of acoustic perturbations at the shock front in the witness will be different than in the sample. For the case where the witness releases into the sample, the Doppler shift between events on the shock front and at the source is

$$\frac{\Delta t_{SFW}}{\Delta t_0} = \frac{1}{1 - M_{S1,d}}, \tag{41}$$

and

$$\frac{\Delta t_{SFS}}{\Delta t_0} = \frac{1+M_{R1,d}}{1+M_{R1,u}} \frac{1}{1-M_{S2,d}}, \tag{42}$$

where the subscripts represent the regions illustrated in Figure 8(b-c). Mach numbers associated with the witness, $M_{S1,d}$, $M_{R1,u}$ and $M_{R1,d}$, are all known from our knowledge of the EOS of the witness material. The Mach number in the sample is determined from the correlation of events at the shock front in the sample and witness. Figure 8(b-c) illustrates how the arrival times of the two perturbations at the window and sample shock front differ, and this difference depends in part on the sound speeds in the materials. Using equations (41) and (42), one may show that downstream of the sample shock front, the Mach number is

$$M_{S2,d} = 1 - \frac{(1-M_{S1,d})(1+M_{R1,d})}{F(1+M_{R1,u})}, \tag{43}$$

where the observable $F = \Delta t_{SFS}/\Delta t_{SFW}$ is the dilation factor. From the definition of the downstream Mach number associated with the sample shock front, the sound speed is defined as

$$c_{s,C1} = \frac{p_{C1}}{u_{p,C1}\rho_{C1}} M_{S2,d}^{-1}. \tag{44}$$

Equations (43) and (44) can be used to extract the sound speed from the ratio of time dilation factors in the transmitted perturbation signals.

The perturbation amplitude in the witness material is,

$$\frac{\delta u_{SFW}}{\delta u_0} = \frac{-2\eta_A}{\eta_A - 1} \frac{M_{S1,d}-1}{1+M_{S1,d}-(\eta_A-1)M_{S1,d}^2\Gamma_{A1,d}}, \tag{45}$$

where $\eta_A = \rho_{A1}/\rho_{A0}$. The corresponding perturbation amplitude in the sample the amplitude is,

$$\frac{\delta u_{SFS}}{\delta u_0} = \frac{2\rho_{B2}c_{s,B2}}{\rho_{B2}c_{s,B2}+\rho_{C1}c_{s,C1}} \frac{-2\eta_C}{\eta_C - 1} \frac{M_{S2,d}-1}{1+M_{S2,d}-(\eta_C-1)M_{S2,d}^2\Gamma_{C1,d}} \tag{46}$$

where $\eta_C = \rho_{C1}/\rho_{C0}$. Except for $\Gamma_{C1,d}$, all quantities on the right-hand sides of the latter two equations are known from the EOS model of the witness, from the known Hugoniot state of the sample, and from equation (43). The observable $G = \delta u_{SFW}/\delta u_{SFS}$ can be combined with equations (43), (45) and (46) to determine the unknown Grüneisen coefficient Γ_{C1} of the sample.

CALE simulations were conducted to test this analytical method. A 50 μm quartz baseplate and quartz witness were used with the EOS defined in Table I. The sample was water and LEOS table 2010 is used.[18] The shock front in both the witness and sample were continuously tracked. The input is a steady 400 GPa pressure drive with two Gaussian impulses peaking at 440 GPa,

separated by 1.3 ns. Using equation (43) and (44) the sound speed in the water was determined to be 12.82 $\pm$ 0.08 km/s compared with the value is 12.79 km/s extracted from the tabular EOS; the uncertainty is associated with resolving the event timing (numerical). The Grüneisen coefficient of the water was determined to be 0.7 $\pm$ 0.2, using equations (45) and (46); this also compares well with the coefficient 0.73 extracted from the tabular model. The uncertainty associated with the Grüneisen coefficient determined from the simulation is partly related to the difficulties of extracting accurate shock front velocity histories as the wave propagates through the numerical mesh (since numerical differentiation is required); this numerical challenge, not present in experiments, is a large contributor in determining δu_{SFW} and δu_{SFS} in this case.

The determination of the sound speed and the Grüneisen coefficient in the shocked material is not limited to the specific case illustrated in Figure 8(b-c); the methods outlined here can be applied more generally, independent of the specific impedance relationship between the witness, baseplate and sample. The primary constraints on experiments designed to determine the sound speed and Grüneisen coefficient from perturbation signals is that the input drive is equivalent for both sections of the target, and that target dimensions and time scales are chosen such that internal reverberations (from the waves reflected at various interfaces) do not reach the drive surface such as to interfere with the perturbation measurement. This design can be extended to study opaque materials, for example, by employing a transparent anvil on the rear surface of the sample. The fluctuating signal transmitted through the opaque sample will be modulated by its response, and by correlating events in both the witness and the anvil the sound speed and Grüneisen coefficient in the opaque material can be inferred. However, when the sample has a higher impedance than the reshock anvil, it would not be possible to determine the Grüneisen coefficient as perturbation amplitude does not dependence upon the sample Grüneisen coefficient.

VI. CONCLUSIONS

We have provided first order accurate formulas and methods to relate pressure perturbations in a shock wave experiment to the observable variations in shock front velocity. The results from the analytical model have been validated with hydrocode simulations. The formulas can be applied when a continuous measurement of the shock velocity in a transparent witness material is available. The acoustic fluctuations in unsteady drive experiments carry information related to derivatives on the mechanical EOS surface. The expressions presented here can be used to extract

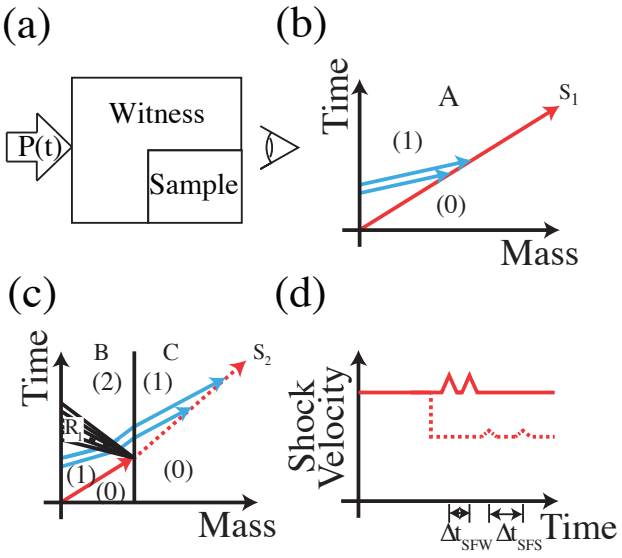

FIG. 8: Illustration of how sound speed can be inferred using using the analytical model presented here. Shock fronts are shown in red and perturbations shown in blue. (A) Target schematic. The EOS of the witness is known. Both the witness and the sample are transparent to the observer and undergo the same loading history. The loading history is steady except for two perturbations. (B) Propagation of the acoustic perturbation (in blue) in the witness. (C) Propagation of the acoustic perturbation through the witness and sample. (D) The arrival times of the acoustic perturbations at the shock fronts in the witness (solid) and in the sample (dashed) depends on the sounds speeds of those materials.

the sound speed and Grüneisen coefficient associated with a shocked state in an unknown sample when a set of velocity measurement data from a common drive source is available for both the sample and a well-calibrated witness material. The method can also be applied to correct for shock wave unsteadiness in impedance-matching analysis, and is well suited for use in laser-based Hugoniot experiments where the shock waves can be unsteady, with fluctuations and/or accelerating or decelerating trends.

Acknowledgments

This work was performed under the auspices of the U.S. Department of Energy by Lawrence Livermore National Laboratory under Contract DE-AC52-07NA27344.

---

[1] C. A. Haynam, P. J. Wegner, J. M. Auerbach, M. W. Bowers, S. N. Dixit, G. V. Erbert, G. M. Heestand, M. A. Henesian, M. R. Hermann, K. S. Jancaitis, K. R. Manes, C. D. Marshall, N. C. Mehta, J. Menapace, E. Moses, J. R. Murray, M. C. Nostrand, C. D. Orth, R. Patterson, R. A. Sacks, M. J. Shaw, M. Spaeth, S. B. Sutton, W. H. Williams, C. C. Widmayer, R. K. White, S. T. Yang, and B. M. Van Wonterghem, "National ignition facility laser performance status," *Appl. Opt.*, vol. 46, no. 16, pp. 3276–3303, 2007.

[2] R. W. Lemke, M. D. Knudson, D. E. Bliss, K. Cochrane, J. P. Davis, A. A. Giunta, H. C. Harjes, and S. A. Slutz, "Magnetically accelerated, ultrahigh velocity flyer plates for shock wave experiments," *Journal of Applied Physics*, vol. 98, no. 7, pp. 073530–9, 2005.

[3] T. R. Boehly, D. L. Brown, R. S. Craxton, R. L. Keck, J. P. Knauer, J. H. Kelly, T. J. Kessler, S. A. Kumpan, S. J. Loucks, S. A. Letzring, F. J. Marshall, R. L. McCrory, S. F. B. Morse, W. Seka, J. M. Soures, and C. P. Verdon, "Initial performance results of the OMEGA laser system," *Optics Communications*, vol. 133, no. 1–6, pp. 495–506, 1997.

[4] J. Neauport, E. Journot, G. Gaborit, and P. Bouchut, "Design, optical characterization, and operation of large transmission gratings for the laser integration line and laser megajoule facilities," *Applied Optics*, vol. 44, no. 16, pp. 3143–3152, 2005.

[5] D. G. Hicks, T. R. Boehly, P. M. Celliers, J. H. Eggert, E. Vianello, D. D. Meyerhofer, and G. W. Collins, "Shock compression of quartz in the high-pressure fluid regime," *Physics of Plasmas*, vol. 12, no. 8, pp. 082702–7, 2005.

[6] M. D. Knudson and M. P. Desjarlais, "Shock compression of quartz to 1.6 TPa: Redefining a pressure standard," *Physical Review Letters*, vol. 103, no. 22, p. 225501, 2009. PRL.

[7] C. F. McMillan, D. R. Goosman, N. L. Parker, L. L. Steinmetz, H. H. Chau, T. Huen, R. K. Whipkey, and S. J. Perry, "Velocimetry of fast surfaces using Fabry–Perot interferometry," *Review of Scientific Instruments*, vol. 59, no. 1, pp. 1–21, 1988.

[8] P. M. Celliers, D. K. Bradley, G. W. Collins, D. G. Hicks, T. R. Boehly, and W. J. Armstrong, "Line-

imaging velocimeter for shock diagnostics at the OMEGA laser facility," *Review of Scientific Instruments*, vol. 75, no. 11, pp. 4916–4929, 2004.

[9] O. T. Strand, D. R. Goosman, C. Martinez, T. L. Whitworth, and W. W. Kuhlow, "Compact system for high-speed velocimetry using heterodyne techniques," *Rev. Sci. Instrum.*, vol. 77, no. 8, p. 083108, 2006.

[10] D. G. Hicks, P. M. Celliers, G. W. Collins, J. H. Eggert, and S. J. Moon, "Shock-induced transformation of Al_2O_3 and LiF into semiconducting liquids," *Physical Review Letters*, vol. 91, no. 3, p. 035502, 2003. PRL.

[11] M. D. Knudson, D. L. Hanson, J. E. Bailey, C. A. Hall, J. R. Asay, and C. Deeney, "Principal hugoniot, reverberating wave, and mechanical reshock measurements of liquid deuterium to 400 GPa using plate impact techniques," *Phys. Rev. B*, vol. 69, p. 144209, Apr 2004.

[12] P. M. Celliers, G. W. Collins, D. G. Hicks, and J. H. Eggert, "Systematic uncertainties in shock-wave impedance-match analysis and the high-pressure equation of state of Al," *Journal of Applied Physics*, vol. 98, p. 113529, 2005.

[13] D. G. Hicks, T. R. Boehly, P. M. Celliers, J. H. Eggert, S. J. Moon, D. D. Meyerhofer, and G. W. Collins, "Laser-driven single shock compression of fluid deuterium from 45 to 220 GPa," *Phys. Rev. B*, vol. 79, p. 014112, Jan 2009.

[14] M. A. Barrios, D. G. Hicks, T. R. Boehly, D. E. Fratanduono, J. H. Eggert, P. M. Celliers, G. W. Collins, and D. D. Meyerhofer, "High-precision measurements of the equation of state of hydrocarbons at 1-10 Mbar using laser-driven shock waves," *Physics of Plasmas (1994-present)*, vol. 17, no. 5, pp. –, 2010.

[15] R. Tipton, R. Managan, and P. Amala, "Cale user's manual," tech. rep., Lawrence Livermore National Laboratory, 2010.

[16] M. D. Knudson and M. P. Desjarlais, "Adiabatic release measurements in α-quartz between 300 and 1200 GPa: Characterization of α-quartz as a shock standard in the multimegabar regime," *Physical Review B*, vol. 88, no. 18, p. 184107, 2013. PRB.

[17] G. R. Gathers, *Selected Topics in Shock Wave Physics and Equation of State Modeling*. New Jersey: World Scientific, 1994.

[18] R. M. More, K. H. Warren, D. A. Young, and G. B. Zimmerman, "A new quotidian equation of state (qeos) for hot dense matter," *Physics of Fluids*, vol. 31, no. 10, pp. 3059–3078, 1988.

[19] R. A. MacDonald and W. M. MacDonald, "Thermodynamic properties of fcc metals at high temperatures," *Physical Review B*, vol. 24, no. 4, pp. 1715–1724, 1981. PRB.

[20] A. C. Mitchell and W. J. Nellis, "Shock compression of aluminum, copper, and tantalum," *Journal of*

Applied Physics, vol. 52, no. 5, pp. 3363–3374, 1981.

[21] G. A. Lyzenga, T. J. Ahrens, W. J. Nellis, and A. C. Mitchell, "The temperature of shock-compressed water," *The Journal of Chemical Physics*, vol. 76, no. 12, pp. 6282–6286, 1982.

[22] M. D. Knudson, M. P. Desjarlais, R. W. Lemke, T. R. Mattsson, M. French, N. Nettelmann, and R. Redmer, "Probing the interiors of the ice giants: Shock compression of water to 700 GPa and 3.8 g/cc," *Physical Review Letters*, vol. 108, no. 9, p. 091102, 2012. PRL.

[23] L. V. Al'tshuler, A. A. Bakanova, A. V. Bushman, I. P. Dudoladov, and V. N. Zubarev, "Evaporation of shock-compressed lead in release waves," *Sov. Phys. JETP*, vol. 46, p. 980, 1977.

[24] N. C. Holmes, "Shock compression of low-density foams," in *High Pressure Science and Technology* (S. Schmidt, J. Shaner, and G. Samara, eds.), pp. 153–156, AIP, New York, 1993.

[25] S. Rothman, K. Parker, C. Robinson, and M. Knudson, "Measurement of a release adiabat from ˜8 Mbar in lead using magnetically driven flyer impact," *Physics of Plasmas*, vol. 11, pp. 5620–5, Dec. 2004.

[26] M. Knudson, J. Asay, and C. Deeney, "Adiabatic release measurements in aluminum from 240- to 500-GPa states on the principal Hugoniot," *Journal of Applied Physics*, vol. 97, pp. 73514–1–14, 1 April 2005.

[27] T. Neal, "Dynamic determinations of the Grüneisen coefficient in aluminum and aluminum alloys for densities up to 6 Mg/m^3," *Phys. Rev. B*, vol. 14, pp. 5172–5181, Dec 1976.

[28] W. J. Nellis, A. C. Mitchell, and D. A. Young, "Equation-of-state measurements for aluminum, copper, and tantalum in the pressure range 80–440 GPa (0.8–4.4 Mbar)," *Journal of Applied Physics*, vol. 93, no. 1, pp. 304–310, 2003.

[29] S. B. Kormer, A. I. Funtikov, V. D. Urlin, and A. N. Kolesnikova, "Dynamic compression of porous metals and the equation of state with variable specific heat at high temperatures," *Sov. Phys. JETP*, vol. 15, pp. 477–88, 1962.

[30] L. V. Al'tshuler, S. B. Kormer, M. I. Brazhnik, L. A. Vladimirov, M. P. Speranskaya, and A. I. Funtikov, "The isentropic compressibility of aluminum, copper, lead, and iron at high pressures," *Sov. Phys.-JETP*, vol. 11, no. 4, p. 766, 1960.

[31] R. G. McQueen, J. W. Hopson, and J. N. Fritz, "Optical technique for determining rarefaction wave velocities at very high pressures," *Review of Scientific Instruments*, vol. 53, no. 2, pp. 245–250, 1982.

[32] The terms "upstream" and "downstream" are used in the context of wave fronts to denote the material regions ahead of and behind the wave front, respectively, when viewed from a reference frame fixed to the front.

[33] Not to be confused with the $+$ and $-$ subscripts in subsection III C. Note that the $+$ and $-$ subscripts in this context refer to wave directions propagating towards and away from the shock front in the downstream region, independent of the shock propagation direction. To avoid confusion the acoustic waves have been labeled in Figure 4.

[34] If $\Delta t_{\text{ref}}/F_{\text{ref}}$ is sufficiently different from $\Delta t_{\text{sample}}/F_{\text{sample}}$ one should compute $\langle u_{\text{W}} \rangle$ separately for the reference correction using the integration interval $[t_1, \Delta t_{\text{ref}}/F_{\text{ref}}]$. An optimized experiment would employ thicknesses of the sample and reference step heights such that both steps experience a common history of perturbations during the transit of the shock through the steps such that $\Delta t_{\text{sample}}/F_{\text{sample}} = \Delta t_{\text{ref}}/F_{\text{ref}}$.